# Insights into primary carbides and nanoparticles in an additively manufactured high-alloy steel

Huayue Zhang [a,*], Hui Peng [b], Paul A.J. Bagot [c], Yiqiang Wang [d], Diego Alba Venero [e], Stuart Robertson [f], Gebril M.A.M. El-Fallah [a], Hongbo Guo [g], Michael P. Moody [c], Bo Chen [a,*]

[a] School of Engineering, University of Leicester, Leicester LE1 7RH, UK
[b] Research Institute for Frontier Science, Beihang University, Beijing 100191, China
[c] Department of Materials, University of Oxford, Oxford OX1 3PH, UK
[d] United Kingdom Atomic Energy Authority, Culham Science Centre, Abingdon OX14 3DB, UK
[e] ISIS Neutron and Muon Facility, Rutherford Appleton Laboratory, Didcot OX11 0QX, UK
[f] Department of Materials, Loughborough University, Leicestershire LE11 3TU, UK
[g] School of Materials Science and Engineering, Beihang University, Beijing 100191, China

## A R T I C L E   I N F O

## A B S T R A C T

This paper reports the use of combined electron microscopy and small-angle neutron scattering (SANS) to probe into the compositional and size evolution of the primary carbides and nanoparticles (defined by a size threshold of 100 nm) in an additively manufactured high-alloy steel before and after heat treatment. The primary carbides exhibit marginal changes in their total volume fraction and size after the austenitising and tempering. However, those carbides located at the prior-austenite boundaries provide a pinning effect to impede grain growth during the austenitising. The grain size increases from 1.7 μm in the as-manufactured to 2.8 μm in the as-tempered conditions, resulting in a limited strength loss of 33–126 MPa as estimated by using the Hall-Petch relationship. Atom probe tomography, which offers atomic spatial resolution examining a sample volume of $6.6 \times 10^5$ nm$^3$, reveals the presence of numerous V and Cr-enriched nanoparticles with sizes of 1 to 10 nm within the steel matrix after the tempering. In contrast, the complementary SANS which examines a significantly larger sample volume of 0.9 mm$^3$ but lacking spatial resolution, provides nanoparticle size information. It reveals a radius reduction from 7.6 to 1.0 nm and a volume fraction increase from 1.6 % to 2.3 %, in the as-manufactured and as-tempered conditions, respectively. The nanoparticles induced during tempering can contribute to a strength enhancement of 691 MPa, primarily through the Orowan bypass mechanism. This suggests that the combination of limited prior-austenite grain growth and the presence of nanoparticles is the key factor responsible for the unprecedented material strength.

## 1. Introduction

A new wave of research on additively manufactured (AM) steels has made major advances in terms of taking full advantage of the unique combination of the solidification rate and thermal gradient [1–4]. For example, 316 L stainless steel processed by laser powder-bed-fusion AM exhibited a considerably improved balance of high strength and ductility when compared to the conventional counterpart [5]. This success was attributed to the AM solidification-induced cellular structures. Nearly all of the AM steel studies [6–13] paid particular attention to the grain or sub-grain level features, crystallographic textures, and their consequent effects on mechanical performance. By contrast, the role of precipitates

on AM steels is far less explored to date. The key findings from the limited amount of previous work are summarised below.

Saewe et al. [14] studied the AM processability and microstructure of HS6–5–3–8 tool steel and its variants with different carbon concentrations. It was found that with the increased carbon, the steel showed reduced hardness from 650±37 Hv (approximately 58 HRC) to 570±31 Hv, despite more carbides being precipitated. They attributed this phenomenon to the carbon-induced stabilisation of the softer retained austenite in the matrix. The work performed by Sander et al. [15] is most likely the first report of the AM tool steel, and they found homogeneously distributed carbides dispersed in a discontinuous network, which was claimed as part of the reason for the high hardness of 900 Hv

---

* Corresponding authors.
*E-mail addresses:* hz202@leicester.ac.uk (H. Zhang), bo.chen@leicester.ac.uk (B. Chen).

(approximately 67 HRC). Greenen et al. [16] studied AM M3:2 tool steel by comparing the laser powder-bed-fusion, hot-isostatic pressing (HIP) and casting materials. In terms of the carbides, the AM steel had the finest particle size of 1 μm; by comparison, 2–5 μm for the HIP steel and 40–100 μm for the cast steel. They also examined the impact of post-processing heat treatment, revealing that the hardness maximum of different states lied relatively close, ranging from 920 to 945 Hv (approximately 68 HRC). Additionally, studies on AM M50 tool steel explored carbides and their evolution during post-processing heat treatment [17–19]. However, these studies along with a handful of works reporting the impact of heat treatment on carbide evolution in AM tool steel [20,21] are mainly focused on the primary carbides within the size range of around 0.7 to 1 μm. Existing research on AM steels lacks in-depth investigation into the relationship between carbides and mechanical properties.

Our previous work on the electron beam powder-bed-fusion AM S390 tool steel revealed unprecedented strength when compared to conventional methods [22]. Compared to the as-manufactured condition, hardness increased from 65 HRC to 73 HRC and the transverse rupture strength increased from 2500 MPa to 3012 MPa after tempering. These superior mechanical properties were attributed to the nanoparticles with a typical size of 21±7 nm. As previously discussed in [23], the non-equilibrium nature of the microstructure induced by AM necessitates additional or adapted post-processing heat treatment for enhanced mechanical properties. This enlightened us to delve deeper into the formation and evolution of nanoparticles with a particular focus on their chemical compositions and size distributions. However, quantifying these extremely fine precipitates poses significant challenges due to the similar atomic numbers of alloying elements (e.g., V, Cr) with Fe.

To achieve the research objective, it is essential to recognise the limitations of individual characterisation techniques and exploit their different strengths. For instance, transmission electron microscopy (TEM) can reveal the microstructure feature as small as 0.1 nm [24], but it lacks the statistical rigour required for quantitative analysis. Conversely, atom probe tomography (APT) is well suited to obtain compositional information with atomic spatial resolution. However, this technique suffers the limitations in volume representativeness [25]. The proposed strategy to tackle the above-mentioned challenge is to employ combined tools. Especially, the present work attempts to use the technique combination of APT and small-angle neutron scattering (SANS) to study the compositional and size evolution of nanoparticles within a high carbon and high alloy steel. These two techniques are considered complementary to each other in the sense that they both cover the same dimensional range [26].

SANS is an emerging technique for characterising precipitation behaviour, and it has proven to be a reliable method to determine both the size and compositional information of the particles with a typical size of less than 100 nm. Leitner et al. [27] studied the precipitates induced by the tempering in HS6–5–2 tool steel using SANS measurement. They reported that the precipitate size derived from SANS was in the same range as those observed by TEM. A similar conclusion was reached by Wang et al. [28] when the SANS technique was used to measure the size distribution of the nanoscale carbides in a vanadium-containing high-strength low-alloy steel. The successful particle characterisation using the SANS technique is not limited to steel research though. Sharma et al. [29] employed the SANS technique to study the isothermal ω-phase evolution in Ti-5553 β-Ti alloy and the determined particle size was consistent with the TEM observation [30]. In terms of the AM domain, Wahlmann et al. [31] used the small-angle X-ray scattering technique (similar to the SANS but based on the synchrotron X-ray beam) to gain new insight into the dynamic behaviour of the γ′-phase during additive manufacturing. To the best of the authors' knowledge, the work of Wahlmann et al. appears as the only attempt to use the small-angle scattering technique to study the nanoparticle behaviour in an AM material.

This paper is devoted to understanding the size and compositional changes of both the primary carbides and nanoparticles under three conditions of the as-manufactured, as-austenitised and as-tempered S390 steel processed by electron-beam powder-bed-fusion. The quantitative analysis of precipitates with distinct compositions in such a complex system is a significant advance in the field. The collected experimental data allows us to critically evaluate the operative strengthening mechanisms, gaining insights into the microstructure-property relationship in AM steels.

## 2. Experimental and data processing

### 2.1. Material

S390 high-alloy steel with a chemical composition of 1.48C-10.34W-2.07Mo-5.08V-4.82Cr-7.98Co-0.58Si-0.23Mn (wt.%) was investigated in this study. The size range of gas-atomised powders was approximately between 45 and 140 μm in diameter. Samples were produced using an Arcam A2XX machine with a power of 330 W, scan velocity of 700 mm/s, line offset of 0.15 mm and layer thickness of 50 μm, resulting in a volumetric energy density of 62.9 J/mm$^3$. The build temperature was maintained at approximately 780 °C over the whole sample fabrication. More details about the electron beam powder-bed-fusion (PBF-EB, also known as selective electron beam melting) additive manufacturing of this steel type can be found elsewhere [22]. The as-manufactured samples with dimensions of 5 × 5 × 10 mm were subjected to austenitising and triple tempering. Fig. 1a schematically shows the heat treatment procedures. The as-austenitised samples were obtained by austenitising at 1230 °C for 4 mins with oil quenching. The as-tempered samples were obtained after the triple tempering at 560 °C for 2 h per each step. Triple tempering was commonly used in high-alloy steels to minimise the amount of retained austenite and promote secondary hardening [32].

### 2.2. Scanning electron microscopy and focused ion beam

Metallographic sample preparation involved grinding and polishing to the final step of 0.25 μm diamond suspensions, followed by chemical etching using 2 % nital. Scanning electron microscopy (SEM) was performed on an FEI Quanta 650 FEG-SEM under back-scattered electron (BSE) imaging mode at 20 keV. The grain size for this material was measured using the linear intercept method [33]. The characteristics of precipitates (fraction and size) were investigated by focused ion beam (FIB) using an FEI Nanolab 600 DualBeam FIB-SEM with etching-assisted gas XeF$_2$ flowing in the chamber. The ion-induced secondary electron micrographs were collected at 30 keV with a current of 50 pA. Statistical particle analysis was performed using Image J [34], based on a total field-of-view area of 200 × 150 μm$^2$ containing more than 1000 particles per carbide type and per material condition. Carbide types were distinguished from each other based on greyscale thresholding. Particles with an area smaller than 0.01 μm$^2$ were filtered to reduce the effect of noise. This was followed by determining their average size in diameter from the equivalent circular area.

### 2.3. Atom probe tomography and transmission electron microscopy

The atomic analysis of precipitates was performed by atom probe tomography (APT). The APT samples were prepared by the lift-out method and were sharpened [35] on a Helios G4 Xe PFIB dual beam system. Final polishing was completed at 2 keV and a beam current of 50 pA. The APT measurements were carried out on a CAMECA LEAP 5000 XR system in laser pulsed mode at a stage temperature of 50 K, a laser power of 100 pJ and a set detection rate of 0.4 %. The data reconstruction was performed using IVAS 3.8.8 software, following a standard protocol [36].

Transmission electron microscopy (TEM) equipped with energy dispersive X-ray spectroscopy (EDS) was used to obtain the compositional and structural information of particles especially those with an
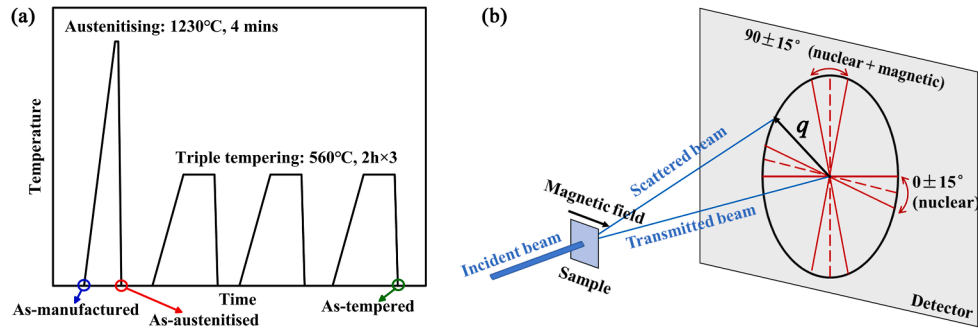
**Fig. 1.** Schematics of (a) heat treatment procedures and three sample conditions; (b) SANS experimental set-up. To obtain the one-dimensional plot of scattering intensity, azimuthal averaging was performed in $\pm 15°$ sectors.

individual size of less than 100 nanometres. A Tecnai F20 was used for this purpose and TEM lamellae were prepared using the FIB method.

### 2.4. Small-angle neutron scattering

Small-angle neutron scattering (SANS) was performed on the ZOOM beamline at the ISIS neutron and muon source, UK, with the experimental setup presented in Fig. 1b. The incident neutron beam of $8 \times 5$ mm was used with a wavelength range from 1.75 to 16.5 Å, covering a $q$ range of 0.004–0.5 Å$^{-1}$. A magnetic field of 1.5 T was applied in the horizontal direction and perpendicular to the neutron beam, Fig. 1b. Each sample with dimensions of $10 \times 5 \times 0.3$ mm (0.3 mm thick) was exposed to the beam for approximately one hour. A polymer reference sample was measured to normalise SANS data to the absolute unit. The reduction of SANS raw data was done using the Mantid software following conventional procedures [37] while the data analysis was performed using the SASfit software [38].

Utilising the SANS technique to determine the nanoparticle size distribution in AM high-alloy steel presents a significant challenge, given the intricate microstructure features, i.e., multiple precipitates coupled with steel matrix. Therefore, data processing deserves further explanation. It has been supposed that the precipitates can be modelled as spherical scatterers in a particle-matrix approach, where the matrix is well described by an exponential decay of the SANS signal as the momentum transfer increases. Therefore, the governing equation of the scattering intensity, $I(q)$, is given below:

$$I(q) = (\Delta\rho)^2 N_0 \int_0^\infty D(R)[V(R)F(q,\ R)]^2 dR + c_0 q^{-c_1} + c_2 \qquad (1)$$

where $q$ is the momentum transfer. $\Delta\rho$ refers to the scattering contrast between the steel matrix and precipitates. $N_0$ is the precipitate number density, $D(R)$ is the normalised size distribution of precipitates with $\int_0^\infty$ $D(R)dR = 1$. $R$ and $V(R)$ are the precipitate radius and its volume. $F(q, R)$ is the form factor. Here, precipitates were assumed to have a spherical shape and a log-normal size distribution. Thus, the form factor and volume are given by:

$$F(q,R) = 3\frac{\sin(qR) - qR\cos(qR)}{(qR)^3} \qquad (2)$$

$$V(R) = \frac{4}{3}\pi R^3 \qquad (3)$$

The number distribution $N(R)$ follows:

$$N(R) = N_0 \cdot D(R) = \frac{N_0}{\sqrt{2\pi}sR}\exp\left\{-\frac{\ln(R/R_0)^2}{2s^2}\right\} \qquad (4)$$

where $R_0$ and $s$ are two fitting parameters, and once their values are determined, the average precipitate size in radius ($R_{mean}$) can be worked out by the relation of $R_{mean} = R_0 e^{\frac{s^2}{2}}$. The total volume fraction of precipitates ($f_v$) is derived from $f_v = \int_0^\infty N(R)V(R)dR$.

The second and third terms of Eq. (1) are the background terms. $c_0 q^{-c_1}$ represents the scattering from those large particle features (e.g., primary carbides) with a size of >150 nm and the matrix, as calculated using the value of $q = 0.004$ Å$^{-1}$, which cannot be determined from the present scattering curve. And the $q$-independent term $c_2$ represents the incoherent background [39]. All the parameters were determined through the nonlinear least squares curve fitting of Eq. (1) to the SANS measured $I(q)$ vs. $q$ dataset. In the fitting process, $N_0(\Delta\rho)^2$ in the first part of Eq. (1) was treated as one parameter due to the highly coupled and inverse relationship between the two [40].

### 3. Results

#### 3.1. Fine particles with a size of >100 nm

Representative BSE micrographs of the as-manufactured, as-austenitised and as-tempered steel sample conditions, are shown in Fig. 2a, 2c and 2e, respectively, revealing the distribution of the carbide particles in the steel matrix. Fig. 2b, 2d, and 2f are enlarged views showing their detailed features. For the as-manufactured condition (Fig. 2a and 2b), carbide particles are distributed at the prior-austenite grain boundaries, forming the discontinuous network. Two types of carbides can be readily distinguished based on their atomic-number contrast: the brighter ones being Mo, W-enriched $M_2C/M_6C$ carbides, while the darker ones as the V-enriched MC carbides. After austenitising (Fig. 2c and 2d), the carbide network disappeared, replaced by the discrete and larger particles. Most particles with polygonal shapes and larger sizes were at the junctions of multiple grains; by contrast, those with round shapes and smaller sizes tended to appear at the grain interiors. After tempering (Fig. 2e and 2f), a high number of finer carbides appeared and their distribution within the grain was comparatively homogeneous. The morphology of carbides at the junctions remained the same.

For statistical analysis of carbide size distribution, ion-induced secondary electron micrographs were used, as opposed to those BSE micrographs. This is because the V-enriched carbide particles had a similar grey scale to the steel matrix, which made automated analysis via Image J software difficult and less reliable. By comparison, the phase contrast was enhanced due to the preferential etching of the steel matrix, aided by the XeF$_2$ gas; refer to [41,42] for more details. The particle boundaries are easily discernible under the ion-induced secondary electron imaging for all three conditions, Fig. 3a–3c. The larger the atomic mass of a compound, the higher the likelihood that ions can interact, yielding more secondary electrons [43]. Thus, grey particles in Fig. 3a–3c are Mo,
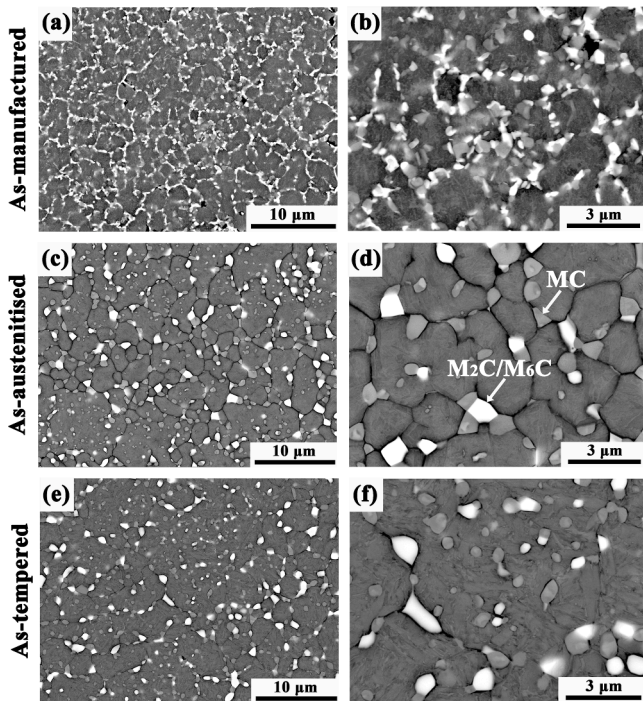
**Fig. 2.** Representative BSE micrographs showing the carbide particles distributed in the steel matrix: (a) and (b) as-manufactured; (c) and (d) as-austenitised; (e) and (f) as-tempered conditions. Note: figures (b), (d) and (f) are the enlarged views of (a), (c) and (e), respectively.

W-enriched $M_2C/M_6C$ carbides while dark particles are V-enriched MC carbides.

Fig. 3d compares the particle size distribution histograms of the as-manufactured, as-austenitised, and as-tempered conditions, respectively, accompanied by the equivalent circle diameter and area fraction along with the standard deviation listed in the figures. Due to the resolution limitation, only particles with diameters larger than 100 nm

were included in the analysis to ensure repeatability. The carbide particles in the as-manufactured sample condition had the smallest average size of 260 nm for MC carbides and 283 nm for $M_2C/M_6C$ particles, while the as-austenitised condition had the largest particle size with 336 nm for MC carbides and 311 nm for the $M_2C/M_6C$. After tempering, the MC size decreased to 301 nm while that of the $M_2C/M_6C$ was unchanged. In terms of the area fraction, the as-austenitised condition had the lowest value of 15.4 %, in comparison with 16.6 % and 16.5 % for the as-manufactured and as-tempered conditions.

### 3.2. Compositions of nanoparticles with a size of ≤100 nm

Fig. 4a shows the APT atom maps of C, Fe, Cr, V, Mo and W for the as-manufactured condition. C, V, Mo and W segregate to form several carbide nanoparticles in the steel matrix with a size of approximately 50 nm. Fig. 4b shows the atomic distribution map of Fe (blue) and C (black), together with the iso-concentration surfaces of 20 at% V in green to delineate the V-enriched carbide particles. Fig. 4c shows the proximity histogram sampling the matrix and into a selected carbide particle located in the middle of the analysed volume. Within the precipitate, the composition is 41 %-V, 30 %-C, 12 %-W, 5.7%-Cr, 5.2%-Mo, 2.8 %-Fe (at.%), confirming its identity as a vanadium rich carbide. Overall, neither the steel matrix nor the carbides show measurable compositional inhomogeneity.

In the as-austenitised condition, all elements in the analysed volume exhibit a homogeneous distribution, Fig. 5a. The atomic distribution map of Fe overlaid with the iso-concentration surfaces of 5 at.% V in green is shown in Fig. 5b, where only one tiny particle with an elongated shape of 20 nm in length but 2 nm thick is visible. This implies that the nano-scale V-enriched carbide particles as observed in the as-manufactured condition (Fig. 4) were dissolved during the austenitising. The proximity histogram in Fig. 5c shows the enrichments of C and V associated with this particle, but their levels are much lower than those as measured in the as-manufactured condition (Fig. 4c). In contrast, the Fe concentration associated with this nanoparticle reaches a value of 40 at.%. This value however could be influenced by possible local magnification effects that can manifest in these types of APT features [36].
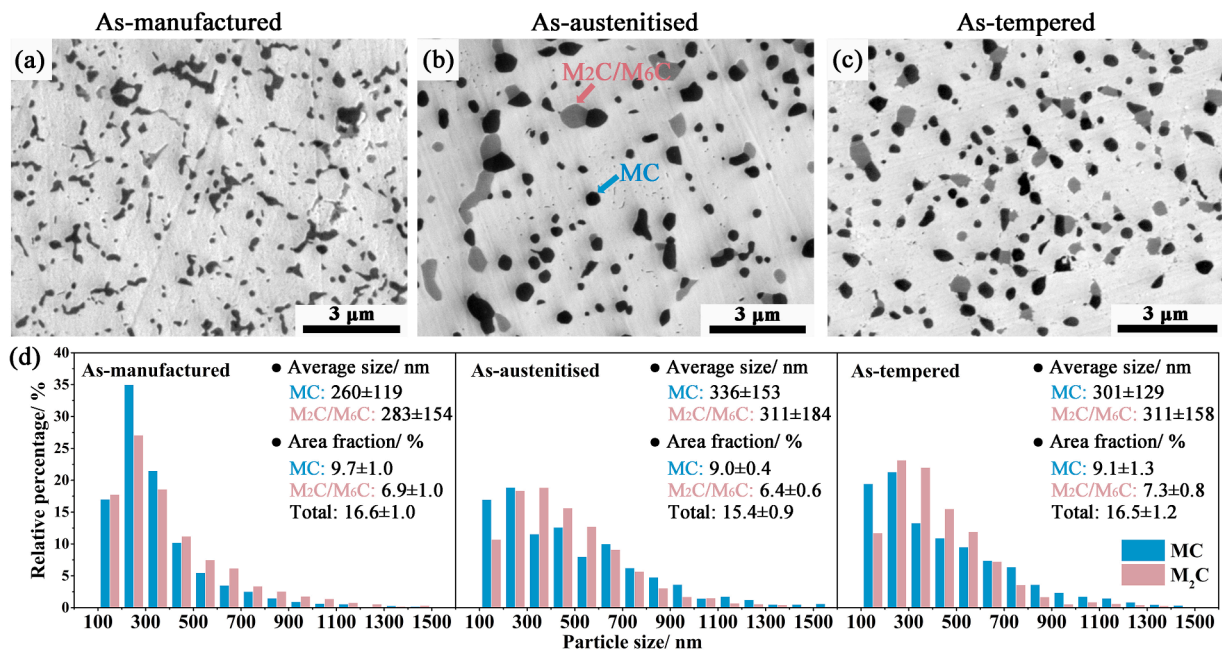


**Fig. 3.** Ion-induced secondary electron micrographs showing the carbide distribution in the steel matrix of (a) as-manufactured, (b) as-austenitised and (c) as-tempered conditions; (d) particle size distribution histograms for MC and $M_2C/M_6C$ carbides. Note: grey particles are $M_2C/M_6C$ carbides and dark particles are MC carbides.
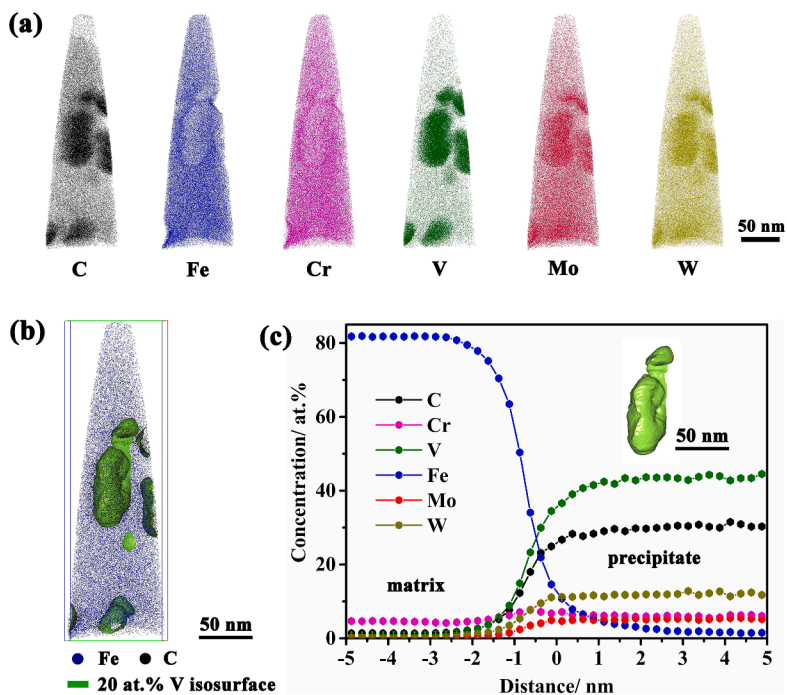
**Fig. 4.** APT analysis of as-manufactured condition: (a) selected atom maps; (b) Fe, C combined atom also showing iso-concentration surface of 20 at.% V; and (c) proximity histograms of key elements across the matrix-carbide interface.
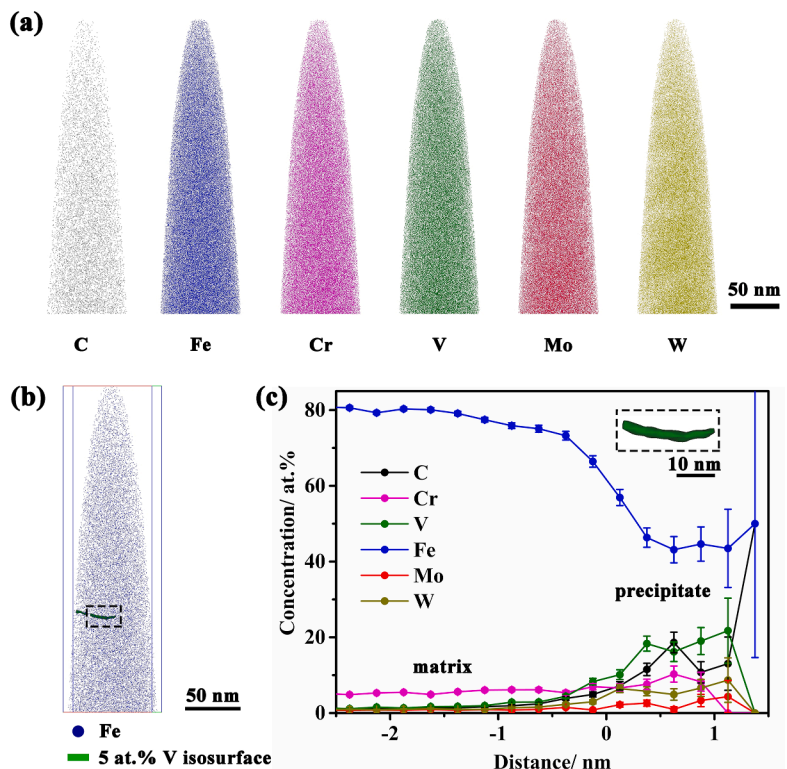


**Fig. 5.** APT analysis of as-austenitised condition: (a) selected element atom maps; (b) 3D reconstruction of volume showing Fe and the iso-concentration surface of 5 at.% V; and (c) proximity histogram across the feature highlighted in (b).

Fig. 6a shows the elemental atom maps of C, Fe, Cr, V, Mo and W for the as-tempered condition. C, V, Mo and W are segregated into discrete regions throughout the analysis volume, indicating the formation of nanoparticles during the tempering. Fig. 6b shows the atomic distribution map of V overlaid with iso-concentration surfaces of V (10 at.%) which highlights numerous V-rich nanoparticles with sizes of 1–10 nm. The proximity histogram in Fig. 6c shows the concentration profile through such a typical particle with its enlarged view shown in the figure inset. This carbide particle has a composition of 25 at.% V, 24 at. % C and 20 at.% Cr, indicating that the nanoparticles in the as-tempered
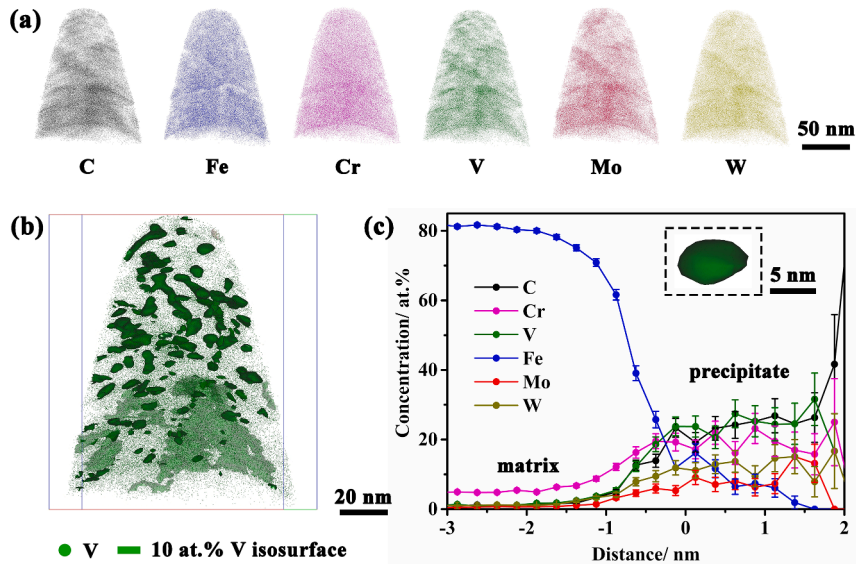
**Fig. 6.** APT analysis of as-tempered condition: (a) selected element atom maps; (b) atom map of V and iso-concentration surface of 10 at.% V; (c) proximity histogram across matrix-carbide interface from the selected particle (as shown in inset).

condition are V and Cr-enriched carbides.

### 3.3. Size distribution of nanoparticles with a size of ≤100 nm

For the present steel, a ferromagnetic material, the applied 1.5 T magnetic field was sufficiently high to saturate the steel matrix. Thus, the scattering contrast $\Delta\rho$ in Eq. (1) can be formulated as:

$$(\Delta\rho)^2 = (\Delta\rho_{nuc})^2 + (\Delta\rho_{mag})^2\sin^2\alpha \qquad (5)$$

where $\alpha$ is the angle between the magnetic field direction and $q$. $\Delta\rho_{nuc}$ is nuclear scattering contrast and $\Delta\rho_{mag}$ stands for the magnetic scattering contrast. Thus, nuclear scattering ($\alpha=0°\pm15°$) was measured on the horizontal plane whereas nuclear + magnetic scattering ($\alpha=90°\pm15°$) on the vertical plane, Fig. 1b. Their subtraction is magnetic scattering contribution. Since more than one type of nanoparticles are expected, the magnetic scattering data was used to derive their total volume fraction ($f_v$) and average radius ($R_{mean}$). The immediate advantage is that $\Delta\rho_{mag}$ in Eq. (5) is equal to the magnetic scattering length density of the steel matrix, $\rho_{mag.m}=5 \times 10^{-6}$ Å$^{-2}$ [28], given the non-magnetic nature of carbides (i.e., V-enriched and V, Cr-enriched nanoparticles). In other words, these non-magnetic nanoparticles act as 'magnetic holes' in the matrix and their magnetic scattering length density is 0. By contrast, it is challenging to derive the nanoparticle information from nuclear scattering data without knowing the value of $\Delta\rho_{nuc}$, because particles of different types would have different nuclear scattering length densities. To this end, analysing those nanoparticles in the present complex alloy system necessitates a novel SANS data analysis approach and its interpretation.

The SANS results obtained from all three sample conditions are presented in Fig. 7a–7c. A $q^{-4}$ plot of Porod's law (the second part of Eq. (1) with the $c_1$ value of 4) is included in each figure to show the expected scattering contribution from larger particles of >150 nm (derived using $q = 0.004$ Å$^{-1}$) on the presently measured $q$ range of 0.004–0.6 Å$^{-1}$. In the as-manufactured condition (Fig. 7a), the scattering intensity $I(q)$ closely followed the $q^{-4}$ behaviour at the low $q$ regime, but it started deviating from the $q^{-4}$ plot at $q > 0.015$ Å$^{-1}$. The magnetic signal was parallel to the nuclear signal and the two showed a marginal difference. In the as-austenitised condition (Fig. 7b), only the nuclear signal followed the $q^{-4}$ behaviour over the entire q-range except for the background regime of $q > 0.1$ Å$^{-1}$. This indicates that the principal contribution to nuclear scattering is from the interface between the steel

matrix and scattering particles. However, the magnetic signal exhibited deviation from the $q^{-4}$ behaviour at $q > 0.01$ Å$^{-1}$. In the as-tempered condition (Fig. 7c), both the nuclear and magnetic intensity plots deviated from Porod's law, at approximately $q > 0.02$ Å$^{-1}$. The observed difference between the nuclear and magnetic scattering data for the as-austenitised and as-tempered conditions will be discussed later.

Fig. 7d illustrates the SANS fitting curve for the as-tempered condition, in comparison with the experimental data. Overall, a reasonably good agreement can be seen. The total fit (red solid line) is the sum of the scattering signal from the nanoparticles (green short dash line) and the power-law plus incoherent background (blue dash line). Fig. 8 compares the size distribution of nanoparticles between the as-manufactured and as-tempered conditions. The peak position of the as-tempered condition was shifted to the left and the peak had a much higher intensity when compared to the as-manufactured condition. This indicates that a large quantity of much smaller particles appeared in the as-tempered condition. The corresponding values of $R_0$ and $s$ are indicated in the figure, from which the two characteristic parameters of $f_v$ and $R_{mean}$ were calculated using Eq. (4). It is noted that the value of scattering length density $\rho_{nuc}$ of precipitates in this steel is unknown. It is extremely challenging to obtain the parameter of volume fraction from nuclear scattering data. The parameter $f_v$ was derived from magnetic scattering data as an approximated value by applying $\Delta\rho_{mag}$ of $5 \times 10^{-6}$ Å$^{-2}$. Table 1 summarises the $R_{mean}$ values determined using both SANS nuclear and magnetic data and $f_v$ values determined using the magnetic data, from three as-manufactured samples and two as-tempered samples. The consistent results across individual sample measurements under the same condition indicate the reliability of the more exploratory SANS technique. The values of $R_{mean}$ obtained from nuclear data are similar to those from magnetic data indicating the reliability of parameter values $f_v$ and $R_{mean}$ derived from magnetic data that were used as the values for discussion. The nanoparticles in the as-manufactured sample had a mean radius of 7.60 nm with a volume fraction of 1.60 %. After the triple tempering heat treatment, the mean radius of nanoparticles reduced to 0.95 nm but the volume fraction increased to 2.32 %.

Under conditions of a saturated steel matrix and the chemical size being the same as the magnetic size, the A-ratio of the nuclear + magnetic to the nuclear scattering intensity, as illustrated by the middle part of Eq. (6), is proportional to the squared ratio of magnetic to nuclear scattering contrast:
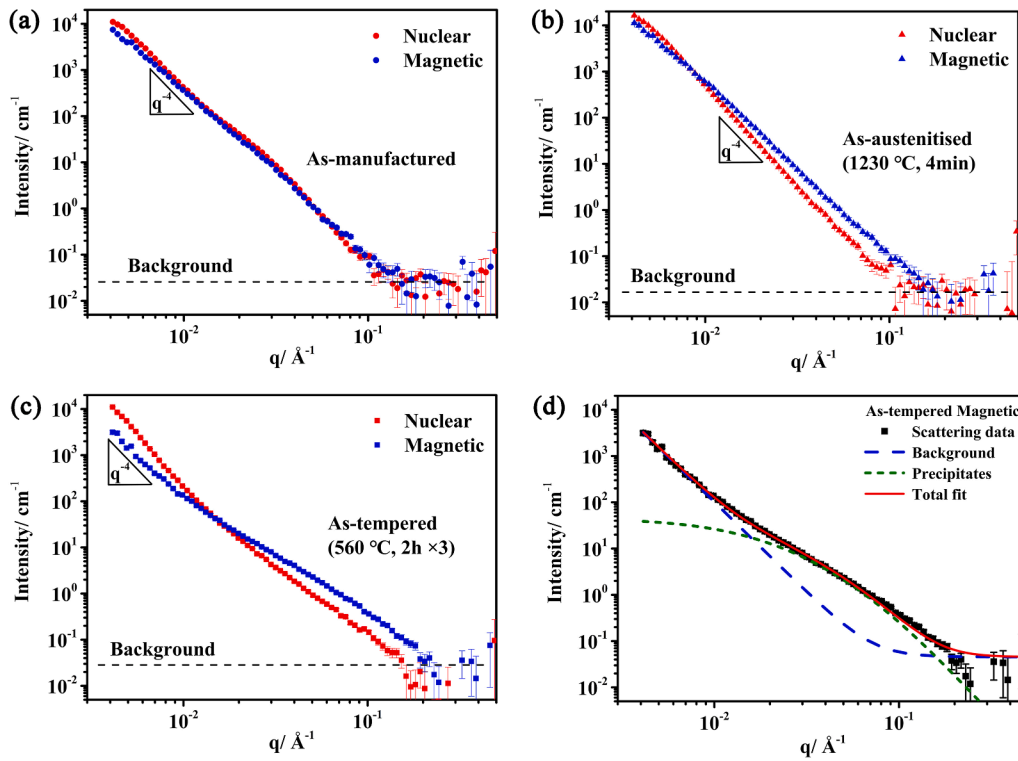
**Fig. 7.** One-dimensional SANS measured intensity $I(q)$ vs. $q$ for three sample conditions in (a)–(c), and the fitting result for the as-tempered sample condition in (d). Data plots of $I(q)$ vs. $q$ for (a) as-manufactured, (b) as-austenitised and (c) as-tempered condition. The lines in (a) to (c) with a slope of −4 indicate Porod's law. Note: magnetic data was obtained by subtracting the measured nuclear from nuclear + magnetic data.
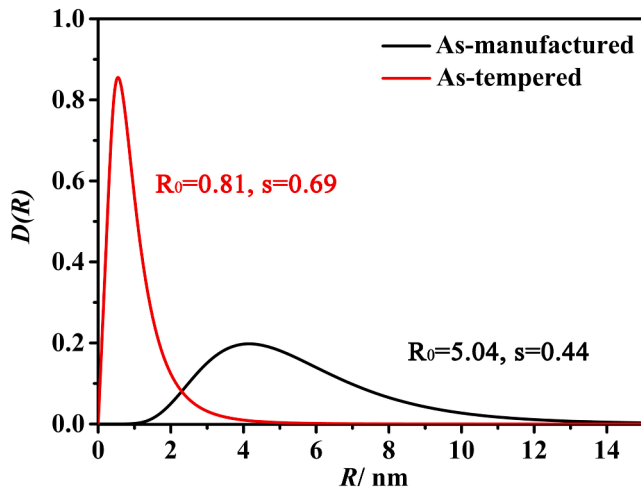


**Fig. 8.** Normalised size distribution plots of $D(R)$ vs. $R$ for the as-manufactured condition (black line) and as-tempered condition (red line) with fitting parameters $R_0$ and $s$ listed in the figure.

$$A(q) = \frac{I_{nuc}(q) + I_{mag}(q)}{I_{nuc}(q)} = 1 + \frac{\Delta\rho^2_{mag}}{\Delta\rho^2_{nuc}} \qquad (6)$$

A-ratio is related to the chemical composition of the precipitates. Fig. 9 compares the A-ratio for the three sample conditions, with the focus on the $q$ range lower than 0.1 Å$^{-1}$. The error bars at the $q$ range higher than 0.1 Å$^{-1}$ are considerably large due to the incoherent background, see the shaded region in Fig. 9. For the as-manufactured condition (black points), the A-ratio did not change much, with a value of around 1.8 to 2. However, the A-ratio exhibited a strong $q$-dependence for both the as-austenitised (orange points) and as-tempered (green points) conditions. Specifically, the A-ratio went up to about 3.8 at $q = 0.05$ Å$^{-1}$. This indicates that the nuclear scattering contrast $\Delta\rho_{nuc}$ changes with the size of nanoparticles, as the magnetic scattering contrast $\Delta\rho_{mag}$ is a fixed value. It is thus hypothesised that more than one type of nanoparticles with different chemical compositions might occur in the as-austenitised and as-tempered conditions. This will be justified next.

**Table 1**

Mean radius and volume fraction of precipitates in as-manufactured and as-tempered conditions, determined using the magnetic scattering data.

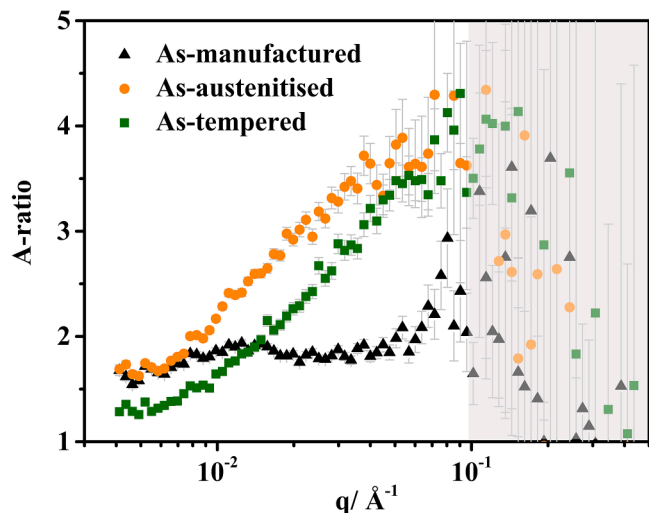| Sample condition | Radius/ nm | | | | Volume fraction/% | |
|---|---|---|---|---|---|---|
| | Individual (Nuclear) | Average | Individual (Magnetic) | Average | Individual (Magnetic) | Average |
| As-manufactured | 6.98 | | 5.55 | | 0.51 | |
| | 10.57 | 8.75±1.80 | 9.60 | 7.60±2.02 | 2.38 | 1.60±0.97 |
| | 8.72 | | 7.65 | | 1.90 | |
| As-tempered | 1.28 | 1.24±0.07 | 1.02 | 0.95±0.11 | 1.39 | 2.32±1.31 |
| | 1.18 | | 0.87 | | 3.24 | |

**Fig. 9.** Plots of A-ratio vs. $q$ as calculated from the SANS data presented in Fig. 7a–7c for all three sample conditions.

## 4. Discussion

### 4.1. Nanoparticles

The nuclear scattering length density can be theoretically calculated with the equation below:

$$\rho_{nuc} = \frac{\Sigma_{i=0}^{n} b_i}{V} \tag{7}$$

where $i$ stands for the individual element for the phase of interest, $b_i$ is the coherent scattering length of each element, and $V$ is the volume of the scatterer. By using the expected stoichiometric ratio, the magnitude of $\rho_{nuc}$ was calculated for the common carbide types in high-alloy steel [44–46]. The calculation was performed using the calculator developed by the NIST Centre for Neutron Research [47] with the input parameters of the chemical formula and mass density.

Table 2 summarises the calculation results in terms of the nuclear scattering length density $\rho_{nuc}$, nuclear scattering contrast $\Delta\rho_{nuc}$, and magnetic scattering contrast $\Delta\rho_{mag}$. Note for the steel matrix, $\rho_{nuc}$ was calculated as $8.0 \times 10^{-6}$ Å$^{-2}$, using the mass density of 7.87 g/cm$^{-3}$ and Fe as the chemical formula. Hence, the column of $\Delta\rho_{nuc}$ is simply the $\rho_{nuc}$-value difference between each carbide type and the steel matrix. Comparison of these theoretical A-ratio values with those derived from the SANS measurements (Fig. 9) can provide further explanations to the chemical compositions of nanoparticles.

For the as-manufactured condition, the A-ratio derived from the SANS measurement is around 1.8 (Fig. 9), which is close to the theoretical value of 2.2 for VC and 1.6 for V$_2$C carbides (Table 2). The deviation in A-ratio from expected stoichiometric compositions might be

**Table 2**
Summary of scattering contrast and calculated A-ratio for different carbides.

| Phase | Density/ g·cm$^{-3}$ | $\rho_{nuc}$ / × 10$^{-6}$ Å$^{-2}$ | $\Delta\rho_{nuc}$ / × 10$^{-6}$ Å$^{-2}$ | $\Delta\rho_{mag}$ / × 10$^{-6}$ Å$^{-2}$ | A-ratio |
|---|---|---|---|---|---|
| VC | 5.77 | 3.43 | 4.59 | | 2.2 |
| MoC | 8.51 | 6.34 | 1.68 | | 9.9 |
| WC | 15.4 | 5.41 | 2.61 | | 4.7 |
| V$_2$C | 5.43 | 1.65 | 6.37 | | 1.6 |
| Mo$_2$C | 8.56 | 5.08 | 2.94 | 5.00 | 3.9 |
| W$_2$C | 16.5 | 4.23 | 3.79 | | 2.7 |
| Cr$_{23}$C$_6$ | 7.30 | 4.28 | 3.74 | | 2.8 |
| Fe$_3$C | 7.70 | 9.04 | 1.04 | | 24.1 |
| Fe$_3$W$_3$C | 14.3 | 5.84 | 2.18 | | 6.3 |

related to the effect of compositions on the parameters in Eq. (7). The identified carbide type is further substantiated by the APT results as presented in Fig. 4. The chemical composition of precipitates as observed by APT contains Mo, Cr, and W elements in addition to C and V, with concentrations of 30.8 at.% C, 6.1 at.% Cr, 44.1 at.% V, 5.0 at.% Mo, and 12.1 at.% W, consistent with a stoichiometry of M$_2$C$_{0.96}$. The volume per atom of M$_2$C carbide can be worked out using the lattice parameters of $a = 2.95$ Å and $c = 4.67$ Å [48]. By using the nominal mass density of 8.9 g/cm$^{-3}$ and under the assumption of a neglected change in the atomic volume due to compositional deviation, the A-ratio for the particle composition of (V$_{1.37}$Cr$_{0.19}$Mo$_{0.16}$W$_{0.38}$)C$_{0.96}$ was calculated as 1.9, which agrees well with the SANS derived A-ratio of 1.8. This suggests that precipitate compositions determined by APT were representative of the bulk information.

For the as-austenitised condition, the $q$-dependent A-ratio behaviour (Fig. 9), along with the lack of scattering signal in the nanoparticle size regime (Fig. 7b), suggests two possible reasons. First, retained austenite (a non-magnetic phase [49]) in the steel matrix can contribute to the $q$-dependent A-ratio behaviour. Second, the presence of Fe-enriched carbides can lead to the $q$-dependent A-ratio, as observed previously by Wang et al. [28] when studying the nanoparticle behaviour of water-quenched steel. The APT result, as shown in Fig. 5, did reveal that the detected tiny carbides contain about 50 at.% Fe. The particle accompanied by C atom segregation could be an undissolved primary carbide particle or a secondary carbide particle precipitated during the quenching process. However, it is noted that such a high Fe concentration could potentially be the artefact of the APT local magnification effects [36]. Leitner et al. [27] reported that the A-ratio increased with the atomic fraction of Fe in the M$_2$C precipitate in high-speed steel in the as-quenched condition. The theoretical calculation results for the Fe$_3$C return an A-ratio value of 24.1 and Fe$_3$W$_3$C carbide has a smaller value of 6.3 (Table 2), which is much higher than the VC and V$_2$C carbides with less atomic fraction of Fe as observed in the as-manufactured condition.

For the as-tempered condition, the A-ratio is $q$-dependent but the value is lower than the as-austenitised condition. This can be attributed to the lower Fe concentration in the tempering induced nanoparticles which contain other carbide-forming elements. The SANS-derived A-ratio is 3.8 which is close to the theoretically calculated A-ratio of 3.9, indicating the Mo$_2$C carbide type. The APT results in Fig. 6 show the presence of V and Cr-enriched nanoparticles, consistent with a stoichiometry of M$_2$C$_{0.91}$. The A-ratio was calculated as 3.1 by using the APT-determined composition of (V$_{0.44}$Cr$_{0.60}$Mo$_{0.35}$W$_{0.34}$Fe$_{0.27}$)C$_{0.91}$, the ideal mass density of 9.1 g/cm$^{-2}$, and the lattice parameters of $a = 2.95$ Å and $c = 4.67$ Å for M$_2$C [48]. It is worth noting that the nanoparticles in the as-tempered condition still contain a fair amount of Fe (9.0 at.%), which can explain the high A-ratio as derived from the SANS measurement.

To provide complementary information about nanoparticles, TEM with EDS operating in scanning transmission electron microscopy (STEM) mode was performed. The bright-field (BF) and high-angle annular dark field (HAADF) images, as shown in Fig. 10a and 10b, reveal the martensite matrix and nanoparticles. EDS mapping (Fig. 10c–10f) of the region shows that the large particle with a diameter of approximately 300 nm, is enriched in V and W. It is important to note one limitation of TEM in the sense that single images lack depth sensitivity [50]. Spectra information is averaged through the lamella thickness. The V, W-enriched particle likely represents an overlapped projection of V-rich MC primary carbides with W-rich M$_6$C carbides. Additionally, EDS mapping of the Cr element (Fig. 10c) indicates tiny Cr-rich particles dispersed in the steel. The TEM results agree with previous APT findings (Fig. 6), confirming the existence of nanoscale Cr-rich secondary carbides after tempering. The V concentration in nanoparticles was lower due to the high V concentration in the adjacent primary carbide. The diameter of nanoparticles as identified through the EDS analysis ranged around 10–20 nm. Any nanoparticles smaller than the above-mentioned size range are challenging to discern due to the
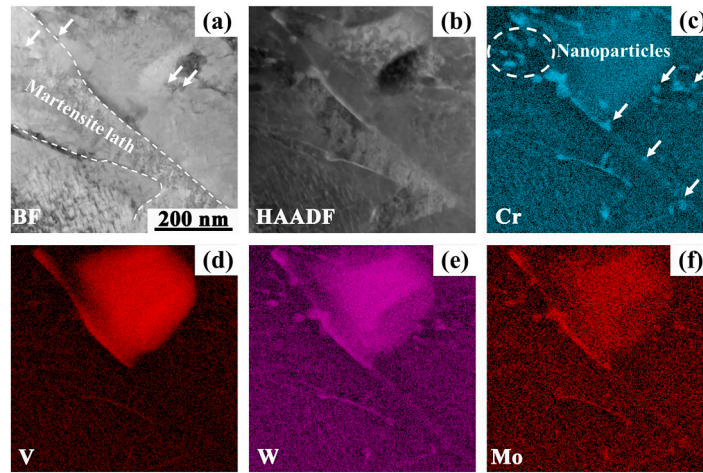
**Fig. 10.** (a) STEM bright-field (BF) image and (b) high-angle annular dark-field (HAADF) images showing the presence of nanoparticles; (c)–(f) Cr, V, W and Mo elemental mappings by STEM-EDS to confirm the Cr-rich characteristics.

noise interference and resolution limitations associated with the technique. This further justifies the importance of using advanced techniques, such as the combination of SANS and APT to overcome the challenge.

### 4.2. Comparison of experimental observation with thermodynamic calculation

Experimentally observed primary carbides and nanoparticles during the rapid solidification are compared with the thermodynamic calculations. Calculations were conducted using JMatPro software (version 12.4) with the General Steel database and chemical composition of 1.48C-10.34W-2.07Mo-5.08V-4.82Cr-7.98Co-0.58Si-0.23Mn (wt.%). For the tempering prediction, the Simultaneous Precipitation module was used to simulate the austenitising temperature of 1230 °C (solution treatment sub-module) and twice tempering (maximum allowable steps in the sub-module) at 560 °C for 2 h each time.

Fig. 11a shows the predicted phase transformations under the non-equilibrium solidification with a cooling rate of $10^6$ K/s. MC and $M_6C$ are the primary carbides formed with the liquid-to-austenite transformation. The formation starting temperatures for the MC and $M_6C$ are 1300 °C and 1272 °C, respectively. More $M_6C$ carbides tend to form with the temperature reduction, accompanied by the lower austenite fraction. At 430 °C, the austenite-to-martensite transformation kicks in, and the
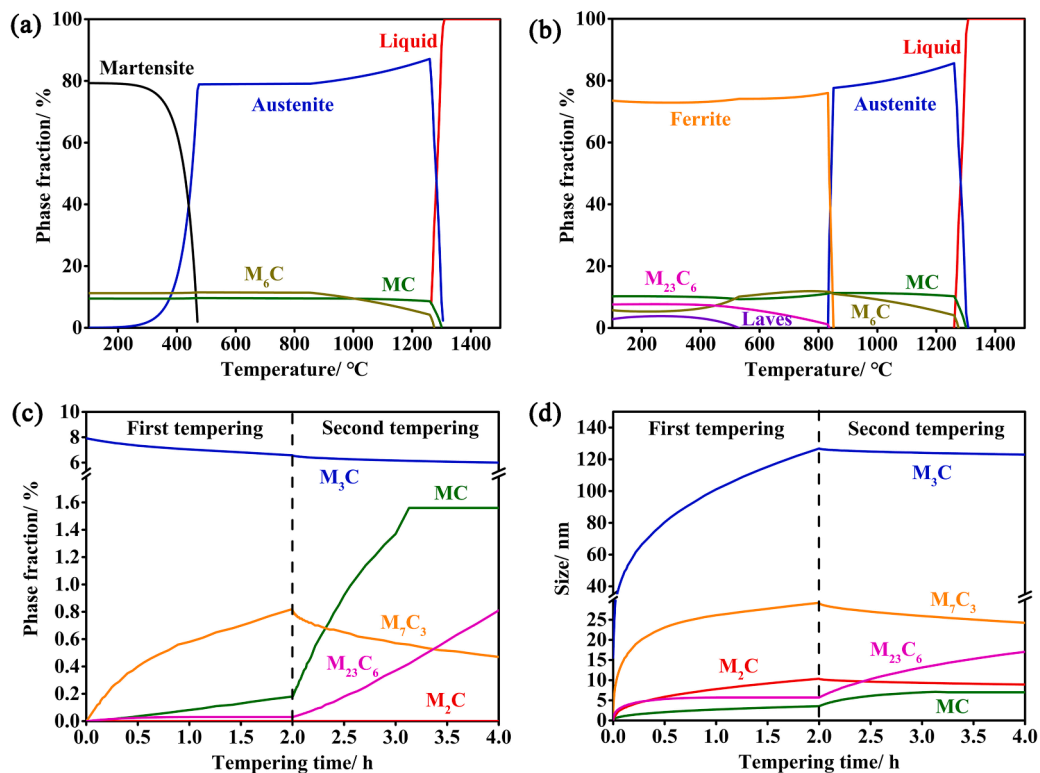


**Fig. 11.** Thermodynamic prediction by JMatPro of (a) phase transformations under the non-equilibrium solidification with a cooling rate of $10^6$ K/s; (b) phase transformations under the equilibrium solidification condition; (c) and (d) the volume fraction and size change of carbides during the tempering heat treatment, respectively.

final phase constitution at room temperature includes martensite, MC and $M_6C$. It is interesting to see the thermodynamic calculation could not predict the $M_2C$ precipitation, even with the use of a cooling rate of $10^6$ K/s. Additive manufacturing with its extremely fast cooling rate ($10^5 \sim 10^7$ K/s [51]) is supposed to create a higher driving force for the $M_2C$ nucleation [52]. Chou et al. [4] calculated the driving force for the carbide precipitation from austenite by performing a solidification simulation under the cooling rate of $5 \times 10^5$ K/s. A higher driving force was found for the formation of $M_2C$ than the $M_6C$. Our previous work on the PBF-EB S390 steel [22] did reveal the presence of $M_2C$ by using transmission electron microscopy. Metastable $M_2C$ decomposes at elevated temperatures, forming MC and $M_6C$ [53]. Moreover, the $M_2C$ carbide also appeared in other additively manufactured high-alloy steels (e.g., H13 [13], M3:2 [16] and M36 [54] grade steels). Therefore, the discrepancy of the $M_2C$ carbide between the thermodynamic calculation and experimental observation deserves future work.

For the PBF-EB process, the entire sample fabrication was performed at the temperature of 780 °C. This means that only part of the non-equilibrium thermodynamic calculations, i.e., above the temperature of 780 °C, is relevant. In other words, information obtained from the equilibrium calculation would be more appropriate for the temperature regime of lower than 780 °C. Fig. 11b presents the thermodynamics calculations under the equilibrium solidification condition. MC and $M_6C$ are the primary carbides formed with the liquid-to-austenite transformation, and their formation starting temperatures are the same as those predicted from the non-equilibrium calculation. $M_{23}C_6$ begins to form at the temperature of 830 °C, which concurs with the austenite-to-ferrite transformation. The Laves phase appears as an equilibrium phase with further cooling. Unfortunately, neither the predicted $M_{23}C_6$ carbide nor the Laves phase was found in our experimental observation.

The modelling executed in JMatPro [55], employing the Scheil-Gulliver model [56,57] for rapid solidification assumes a fast solute diffusion in the liquid phase and a negligible diffusion in the solid phase. The diffusion of C atoms is considered sufficiently fast even in the solid phase. Consequently, the liquid phase was treated as homogeneous in the thermodynamic calculation, assuming local equilibrium at the liquid/solid interface. However, when the liquid/solid interface moves quickly in the rapid solidification process, there is insufficient time for solute elements to diffuse and redistribute within the liquid phase. The swift interface movement results in the solute elements trapping, leading to discontinuities of chemical potential and a loss of equilibrium at the interface. It has been widely observed the element micro-segregation at the dendrite boundaries or cell walls in AM alloy microstructures [58, 59]. The discrepancy in the $M_2C$ phase between the experimental and modelling data could be accounted for by the fact of overlooking the diffusional effects of solute elements, as a result of the simplification of the Scheil-Gulliver model. For the equilibrium calculations, MC and $M_6C$ are predicted to precipitate directly from the liquid phase, while $M_{23}C_6$ is formed later from the solid phase (Fig. 11b). However, equilibrium calculation does not account for the precipitation kinetics. During the rapid solidification and cooling to the chamber temperature, alloying elements were segregated at grain boundaries [23]. V, Mo and W in the steel depleted carbon resources due to the formation of MC and $M_2C/M_6C$ carbides, inhibiting the formation of $M_{23}C_6$ [60]. The Laves phase has been reported to precipitate on martensite lath boundaries or in the adjacent region of $M_{23}C_6$ carbides after long enough annealing (e. g. 204 h at 650 °C [61], 2400 h at 550 °C [62]), suggesting it is not possible to form in the steel after the AM process.

According to the thermodynamic calculations (Fig. 11a and 11b), at the temperature of 1230 °C used for the austenitising treatment, the vast majority of the phase is expected to be austenite. The model prediction agrees reasonably well with the experimental observation. Especially, the predicted total carbide fraction is 15.2 % under the equilibrium condition as compared to 15.4 %±0.9 % from the experimental data (Fig. 3). Despite the carbide dissolution during the austenitising, a small number of undissolved carbides remain at prior-austenite grain

boundaries (Fig. 2a for the as-manufactured and Fig. 2c for the as-austenitised conditions). These undissolved carbides likely helped to hinder the grain boundary motion and control the grain growth. The prior-austenite grain size in the as-austenitised condition was measured as $2.8 \pm 0.6$ μm, which is similar to the size of $1.7 \pm 0.5$ μm for the as-manufactured condition. The disordered arrangement of grain boundary atoms facilitates the diffusion of carbon and alloy elements [63]. In the early stage of quenching, carbon and alloy atoms near the grain boundaries would preferentially segregate towards those undissolved carbides [64], resulting in their size increase as measured in the as-austenitised condition (Fig. 3). A tiny nanoparticle with a length of 20 nm and 2 nm thick was observed by APT (Fig. 5b). This can be interpreted as a partially dissolved particle or a new one formed via re-precipitation during the oil quenching. However, a precipitate with such a high aspect ratio (i.e., the ratio of length over thickness) is very unlikely to form during cooling as the shape is not thermodynamically favourable [65].

Fig. 11c shows the volume fraction change of carbides during the tempering heat treatment. $M_3C$ forms at the very beginning of the first tempering. Although $M_3C$ is not experimentally observed in the present work, Nurbanasari et al. [66] reported the presence of $M_3C$ carbides in the H21 tool steel during tempering. The formation of $M_3C$ carbides can be attributed to the rapid carbon diffusion given the low diffusivity of the substitutional alloying elements [67]. With further tempering, the $M_3C$ fraction reduces, accompanied by the continuously increased $M_7C_3$, MC and $M_{23}C_6$ carbides, among which the precipitation rate of $M_7C_3$ is the fastest. In the subsequent second tempering, the phase fraction of MC carbides increases at the fastest rate, followed by the $M_{23}C_6$ which is transformed from the $M_7C_3$. More details on the carbide transformation of $M_7C_3$ to $M_{23}C_6$ during tempering can be found in [68]. $M_3C$ and $M_7C_3$ are metastable precipitates in the present steel system with their volume fraction decreased during the second tempering. MC and $M_{23}C_6$ are the predominant precipitates after tempering. In addition, the volume fraction of MC becomes unchanged after tempering for 3 h. Cr is a predominant alloy element in the $M_{23}C_6$ [69]. This seems to agree with our APT results for the as-tempered condition (Fig. 6) which shows the increased Cr concentration in those nanoparticles.

In terms of the particle size evolution of precipitates (Fig. 11d), the size of MC which has the highest fraction among the nano-scaled carbides is ~5 nm. The size of $M_{23}C_6$ which has the second highest fraction is ~15 nm. $M_2C$ carbide has a final size of ~10 nm but its volume fraction is extremely low (Fig. 11c). Although the precipitate size is supposed to further increasing with the third tempering, the growth rate would be quite low (<5 nm/h), according to the slope determined close to the 4 h tempering time of Fig. 11d. Overall, the prediction agrees with our experimental data. For example, the APT observed nanoparticles in the as-tempered condition are V and Cr-enriched carbides (Fig. 6) with a size of 1–10 nm.

### 4.3. Strengthening mechanisms

Part of the motivation behind this work is to reconcile the ultra-high strength as observed in the PBF-EB S390 steel (65 HRC in the as-manufactured and 73 HRC in the as-tempered condition [22]), which appears to be unprecedented with reference to the S390 steel processed by conventional means in the as-tempered condition (62 to 68 HRC [70]). With the help of advanced characterisation techniques, key microstructure features have been quantitatively measured: (i) grain size increase from 1.7 μm to 2.8 μm[1] and (ii) nanoparticle volume fraction increase from 1.6 % to 2.3 % accompanied by the size decrease from 7.60 nm to 0.95 nm, when comparing the as-manufactured with the as-tempered sample condition. This section is devoted to linking the

---

[1] Powder metallurgy S390 steel has a prior-austenite grain size of 4~6 μm [70]

microstructure features with material strength.

Grain boundary strengthening can be calculated using the Hall-Petch equation [71,72]:

$$\Delta\sigma_{GB} = k \cdot d^{-\frac{1}{2}} \tag{8}$$

where $k$ is the Hall-Petch coefficient and $d$ is the average grain size. The magnitude of $k$ is known to be material-dependent, but it was not possible to locate such information for the present steel. As a result, upper and lower bound values of $k = 0.74$ MPa•m$^{1/2}$ for mild steel [73] and $k = 0.2$ MPa•m$^{1/2}$ for multi-component ultra-high strength steel [74] were used to estimate the grain boundary strengthening contribution. The $\Delta\sigma_{GB}$ magnitude for the as-manufactured condition was calculated as 153–568 MPa, while 120–442 MPa for the as-tempered condition. This led to the loss of material strength with a level of 33–126 MPa due to the grain size increase from 1.7 μm to 2.8 μm.

The strength contribution from nanoparticles can be assessed by using either the particle shearing or Orowan bypassing strengthening mechanism, depending on the interaction between precipitates and moving dislocations [75–77]. For the precipitates that are coherent with the matrix and with their size smaller than the critical value, dislocations can cut through the precipitates under the shearing mechanism. When the precipitate size exceeds the critical value, ordinarily dislocations bypass the impeding particles by the expansion of the open loops between particles, so-called Orowan bypass mechanism. Note such a mechanism can also operate for the particles that are incoherent with the matrix.

For the particle shearing mechanism, two main influencing factors are the modulus and coherency. The modulus strengthening $\Delta\sigma_{modulus}$ originates from the modulus mismatch between the precipitate and matrix that leads to a change in dislocation tension energy. The coherency strengthening $\Delta\sigma_{coherency}$ is based on the interaction of dislocations with the strain field induced by the lattice misfit between the coherent precipitates and matrix.

The magnitude of modulus strengthening contribution can be calculated by [78]:

$$\Delta\sigma_{modulus} = M \cdot 0.0055 (\Delta G)^{\frac{3}{2}} \left(\frac{2f}{G}\right)^{\frac{1}{2}} \left(\frac{r}{b}\right)^{\frac{3m}{2}-1} \tag{9}$$

where $M$ is the Taylor factor with a value of 2.73 for a body-centred cubic (bcc) polycrystal [79], $b$ is the Burgers vector with a value of 0.25 nm for the bcc-Fe, and $m$ is a constant of 0.85 [76]. $G$ is the shear modulus of the matrix (77 GPa for bcc-Fe [80]). The modulus difference between the matrix and precipitates is symbolised as $\Delta G$ (185 GPa for V-enriched MC carbides [81], whilst 140 GPa and 125 GPa for Cr-enriched $M_{23}C_6$ and $M_7C_3$ carbides [82,83], respectively). $r$ and $f$ are the average size and volume fraction of precipitates, respectively, and their values are obtained directly from the present work. The coherency strengthening can be evaluated by the following equation [76]:

$$\Delta\sigma_{coherency} = M \cdot \chi (G\varepsilon)^{\frac{3}{2}} \left(\frac{rf}{0.5Gb}\right)^{\frac{1}{2}} \tag{10}$$

where $\chi$ is a constant with a value of 2.6 [76]; $\varepsilon = \frac{2}{3}\left|\frac{a_p - a_m}{a_m}\right|$ is the constrained lattice parameter misfit in which $a_p$ is the lattice parameters of the precipitates (0.417 nm for MC carbides [84], 1.059 nm for $M_{23}C_6$ carbides [85], 0.695 nm for $M_7C_3$ carbides [86]) and $a_m$ is the lattice of the matrix (0.288 nm for the S390 steel matrix [22]). For the Orowan bypass mechanism, the modified equation by Gladman [87] based on the original Ashby-Orowan equation [88] is used:

$$\Delta\sigma_{Orowan} = 0.538 \frac{Gbf^{\frac{1}{2}}}{2r} \cdot \ln\left(\frac{r}{b}\right) \tag{11}$$

To estimate the strength increment from the precipitates in the steel, the operative mechanism must be first identified. The strength

increment from the shearing mechanism $\Delta\sigma_{modulus} + \Delta\sigma_{coherency}$ were plotted as a function of radius $r$ according to Eqs. (9) and (10) by applying the respective values of the MC, $M_{23}C_6$ and $M_7C_3$ carbides. A similar plotting was done for the Orowan bypass mechanism $\Delta\sigma_{Orowan}$ by using Eq. (11). Fig. 12 shows the predicted strength increments with the volume fraction set as 1 %. Note using a different value of the volume fraction would only shift the curves up and down in proportion, but it would not change the curve shape, nor their relative positions (unless the volume fraction becomes over 78.5 % which does not apply to the present study). It can be seen that the shearing mechanism (i. e., $\Delta\sigma_{modulus} + \Delta\sigma_{coherency}$) are nearly three orders of magnitude greater than the Orowan mechanism. This means that the dominant strengthening mechanism in the present steel system is the Orowan bypass. Accordingly, the strength increment due to nanoparticles was calculated as 294 MPa and 985 MPa using Eq. (11) together with measured data as shown in Table 1 for the as-manufactured and as-tempered conditions, respectively. Thus, the material strength loss estimated as 33–126 MPa due to the grain growth is compensated for by the nanoparticle-induced Orowan type strengthening mechanism that contributes a strength enhancement of 691 MPa. To this end, precipitation strengthening is believed as the predominant mechanism responsible for the unprecedented strength in the as-tempered PBF-EB high-alloy steel.

## 5. Conclusions

This work focuses on the precipitation behaviour of an additively manufactured high-alloy steel, by gathering the particle size and compositional information with a balanced atomic spatial resolution and statistical rigour. The objective is to elucidate the role of precipitates in material strength by comparing heat-treated and as-manufactured sample conditions. This goal has been achieved using a combination of techniques including ion-induced secondary electron imaging, atom probe tomography (APT) and small-angle neutron scattering (SANS). The following conclusions can be drawn:

1. Primary carbides defined with a size threshold of >100 nm form a discontinuous network at the prior-austenite grain boundaries in the as-manufactured condition. These carbides are important as they can act as pinning points to constrain the grain growth during the austenitising and triple tempering.
2. In terms of nanoparticles, the as-manufactured sample is characterised by the presence of V-enriched particles with a size exceeding 50 nm, whilst the as-tempered sample is characterised by the V and Cr-enriched particles with a size of less than 10 nm and
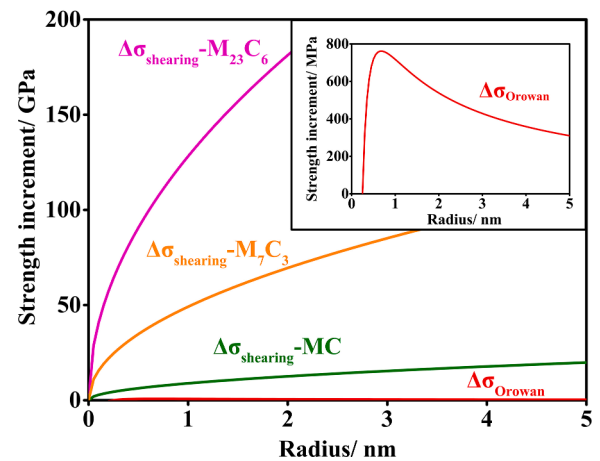


**Fig. 12.** Predicted strength increments as a function of the particle radius, by taking into account the shearing mechanism for three types of precipitates and the Orowan bypass mechanism. The enlarged view at the top right corner shows the Orowan bypass mechanism with the vertical axis unit of MPa.

homogeneously distributed in the steel matrix. The nanoparticle radius reduces from 7.6 to 0.95 nm but volume fraction increases from 1.6 % to 2.3 %. The nanoparticle induced strength enhancement is estimated to be 691 MPa based on the Orowan bypass mechanism.

3. Discrepancies between the experimental data and thermodynamic calculations identify opportunities for further improvement, e.g., the interplay between the three $M_{23}C_6$, $M_3C$ and $M_7C_3$ carbides, which only appeared under the model prediction, and those experimentally observed primary carbides and nanoparticles falling into the group of MC, $M_2C/M_6C$ and possibly $M_{23}C_6$.

## Declaration of competing interest

The authors declare that they have no known competing financial interests or personal relationships that could have appeared to influence the work reported in this paper.

## Acknowledgements

## References

[1] A.T. Polonsky, W.C. Lenthe, M.P. Echlin, V. Livescu, G.T. Gray, T.M. Pollock, Solidification-driven orientation gradients in additively manufactured stainless steel, Acta Mater. 183 (2020) 249–260.

[2] G.T. Gray, V. Livescu, P.A. Rigg, C.P. Trujillo, C.M. Cady, S.R. Chen, J.S. Carpenter, T.J. Lienert, S.J. Fensin, Structure/property (constitutive and spallation response) of additively manufactured 316L stainless steel, Acta Mater. 138 (2017) 140–149.

[3] R. Seede, D. Shoukr, B. Zhang, A. Whitt, S. Gibbons, P. Flater, A. Elwany, R. Arroyave, I. Karaman, An ultra-high strength martensitic steel fabricated using selective laser melting additive manufacturing: densification, microstructure, and mechanical properties, Acta Mater. 186 (2020) 199–214.

[4] C.Y. Chou, N.H. Pettersson, A. Durga, F. Zhang, C. Oikonomou, A. Borgenstam, J. Odqvist, G. Lindwall, Influence of solidification structure on austenite to martensite transformation in additively manufactured hot-work tool steels, Acta Mater. 215 (2021) 117044.

[5] Y.M. Wang, T. Voisin, J.T. McKeown, J. Ye, N.P. Calta, Z. Li, Z. Zeng, Y. Zhang, W. Chen, T.T. Roehling, R.T. Ott, M.K. Santala, P.J. Depond, M.J. Matthews, A. V. Hamza, T. Zhu, Additively manufactured hierarchical stainless steels with high strength and ductility, Nat. Mater. 17 (1) (2018) 63–71.

[6] P. Kumar, Z. Zhu, S.M.L. Nai, R.L. Narayan, U. Ramamurty, Fracture toughness of 304L austenitic stainless steel produced by laser powder bed fusion, Scr. Mater. 202 (2021) 114002.

[7] Z. Wang, T.A. Palmer, A.M. Beese, Effect of processing parameters on microstructure and tensile properties of austenitic stainless steel 304L made by directed energy deposition additive manufacturing, Acta Mater. 110 (2016) 226–235.

[8] X. Wang, B. Zheng, K. Yu, S. Jiang, E.J. Lavernia, J.M. Schoenung, The role of cell boundary orientation on mechanical behavior: a site-specific micro-pillar characterization study, Addit. Manuf. 46 (2021).

[9] L.E. Rännar, A. Koptyug, J. Olsén, K. Saeidi, Z. Shen, Hierarchical structures of stainless steel 316L manufactured by Electron Beam Melting, Addit. Manuf. 17 (2017) 106–112.

[10] Y. Zhong, L.E. Rännar, L. Liu, A. Koptyug, S. Wikman, J. Olsen, D. Cui, Z. Shen, Additive manufacturing of 316L stainless steel by electron beam melting for nuclear fusion applications, J. Nucl. Mater. 486 (2017) 234–245.

[11] J. Olsén, Z. Shen, L. Liu, A. Koptyug, L.E. Rännar, Micro- and macro-structural heterogeneities in 316L stainless steel prepared by electron-beam melting, Mater. Charact. 141 (2018) 1–7.

[12] I.A. Segura, J. Mireles, D. Bermudez, C.A. Terrazas, L.E. Murr, K. Li, V.S.Y. Injeti, R. D.K. Misra, R.B. Wicker, Characterization and mechanical properties of cladded stainless steel 316L with nuclear applications fabricated using electron beam melting, J. Nucl. Mater. 507 (2018) 164–176.

[13] M. Åsberg, G. Fredriksson, S. Hatami, W. Fredriksson, P. Krakhmalev, Influence of post treatment on microstructure, porosity and mechanical properties of additive manufactured H13 tool steel, Mater. Sci. Eng. A 742 (2019) 584–589.

[14] J. Saewe, N. Carstensen, P. Kürnsteiner, E.A. Jägle, J.H. Schleifenbaum, Influence of increased carbon content on the processability of high-speed steel HS6-5-3-8 by laser powder bed fusion, Addit. Manuf. 46 (2021) 102125.

[15] J. Sander, J. Hufenbach, L. Giebeler, H. Wendrock, U. Kühn, J. Eckert, Microstructure and properties of FeCrMoVC tool steel produced by selective laser melting, Mater. Des. 89 (2016) 335–341.

[16] K. Geenen, A. Röttger, F. Feld, W. Theisen, Microstructure, mechanical, and tribological properties of M3:2 high-speed steel processed by selective laser melting, hot-isostatic pressing, and casting, Addit. Manuf. 28 (2019) 585–599.

[17] J. Saewe, C. Gayer, A. Vogelpoth, J.H. Schleifenbaum, Feasability investigation for laser powder bed fusion of high-speed steel AISI M50 with base preheating system, BHM Berg Hüttenmännische Monatshefte 164 (3) (2019) 101–107.

[18] J. Kunz, J. Saewe, S. Herzog, A. Kaletsch, J.H. Schleifenbaum, C. Broeckmann, Mechanical properties of high-speed steel AISI M50 produced by laser powder bed fusion, Steel Res. Int. 91 (5) (2020) 1900562.

[19] S. Qin, S. Herzog, A. Kaletsch, C. Broeckmann, Effects of pressure on microstructure and residual stresses during hot isostatic pressing post treatment of AISI M50 produced by laser powder-bed fusion, Metals 11 (4) (2021) 596.

[20] C. Botero, M. Ramsperger, A. Selte, K. Åsvik, A. Koptyug, P. Skoglund, S. Roos, L. E. Rännar, M. Bäckström, Additive manufacturing of a cold-work tool steel using electron beam melting, Steel Res. Int. 91 (5) (2020) 1900448.

[21] F. Großwendt, A. Röttger, A. Strauch, A. Chehreh, V. Uhlenwinkel, R. Fechte-Heinen, F. Walther, S. Weber, W. Theisen, Additive manufacturing of a carbon-martensitic hot-work tool steel using a powder mixture – Microstructure, post-processing, mechanical properties, Mater. Sci. Eng. A 827 (2021) 142038.

[22] J. Jin, R. Gao, H. Peng, H. Guo, S. Gong, B. Chen, Rapid solidification microstructure and carbide precipitation behavior in electron beam melted high-speed steel, Metall. Mater. Trans. A 51 (5) (2020) 2411–2429.

[23] P. Bajaj, A. Hariharan, A. Kini, P. Kürnsteiner, D. Raabe, E.A. Jägle, Steels in additive manufacturing: a review of their microstructure and properties, Mater. Sci. Eng. A 772 (2020) 138633.

[24] D.B. Williams, Electron microscopy: transmission, in: K.H.J. Buschow, R.W. Cahn, M.C. Flemings, B. Ilschner, E.J. Kramer, S. Mahajan, P. Veyssière (Eds.). Encyclopedia of Materials: Science and Technology, Elsevier, Oxford, 2001, pp. 2577–2584.

[25] B. Gault, A. Chiaramonti, O. Cojocaru-Mirédin, P. Stender, R. Dubosq, C. Freysoldt, S.K. Makineni, T. Li, M. Moody, J.M. Cairney, Atom probe tomography, Nat. Rev. Methods Primers 1 (1) (2021) 51.

[26] T.H. Simm, L. Sun, D.R. Galvin, E.P. Gilbert, D. Alba Venero, Y. Li, T.L. Martin, P.A. J. Bagot, M.P. Moody, P. Hill, H.K.D.H. Bhadeshia, S. Birosca, M.J. Rawson, K. M. Perkins, A SANS and APT study of precipitate evolution and strengthening in a maraging steel, Mater. Sci. Eng. A 702 (2017) 414–424.

[27] H. Leitner, P. Staron, H. Clemens, S. Marsoner, P. Warbichler, Analysis of the precipitation behaviour in a high-speed steel by means of small-angle neutron scattering, Mater. Sci. Eng. A 398 (1) (2005) 323–331.

[28] Y.Q. Wang, S.J. Clark, V. Janik, R.K. Heenan, D.A. Venero, K. Yan, D.G. McCartney, S. Sridhar, P.D. Lee, Investigating nano-precipitation in a V-containing HSLA steel using small angle neutron scattering, Acta Mater. 145 (2018) 84–96.

[29] D. Sharma, D. Parfitt, B. Chen, B. Roebuck, D.A. Venero, S.R. Kada, D. Fabijanic, M. E. Fitzpatrick, Influence of cooling rate on the precipitation kinetics of nanoscale isothermal ω-phase in metastable β-Ti alloy, Ti–5Al–5Mo–5V–3Cr, J. Alloys Compd. 859 (2021) 157822.

[30] P. Zháňal, P. Harcuba, M. Hájek, B. Smola, J. Stráský, J. Šmilauerová, J. Veselý, M. Janeček, Evolution of ω phase during heating of metastable β titanium alloy Ti–15Mo, J. Mater. Sci. 53 (1) (2018) 837–845.

[31] B. Wahlmann, F. Galgon, A. Stark, S. Gayer, N. Schell, P. Staron, C. Körner, Growth and coarsening kinetics of gamma prime precipitates in CMSX-4 under simulated additive manufacturing conditions, Acta Mater. 180 (2019) 84–96.

[32] W.E. Bryson, The Heat-Treating Processes Step 4: Tempering, Heat Treatment, Carl Hanser Verlag GmbH & Co. KG, Munich, 2015, pp. 108–111.

[33] A. Thorvaldsen, The intercept method—2. Determination of spatial grain size, Acta Mater. 45 (2) (1997) 595–600.

[34] C.A. Schneider, W.S. Rasband, K.W. Eliceiri, NIH Image to ImageJ: 25 years of image analysis, Nat. Methods 9 (7) (2012) 671–675.

[35] M.K. Miller, K.F. Russell, Atom probe specimen preparation with a dual beam SEM/FIB miller, Ultramicroscopy 107 (9) (2007) 761–766.

[36] M.K. Miller, R.G. Forbes, Atom probe tomography, Mater. Charact. 60 (6) (2009) 461–469.

[37] O. Arnold, J.C. Bilheux, J.M. Borreguero, A. Buts, S.I. Campbell, L. Chapon, M. Doucet, N. Draper, R. Ferraz Leal, M.A. Gigg, V.E. Lynch, A. Markvardsen, D. J. Mikkelson, R.L. Mikkelson, R. Miller, K. Palmen, P. Parker, G. Passos, T. G. Perring, P.F. Peterson, S. Ren, M.A. Reuter, A.T. Savici, J.W. Taylor, R.J. Taylor, R. Tolchenov, W. Zhou, J. Zikovsky, Mantid–Data analysis and visualization package for neutron scattering and μ SR experiments, Nucl. Instrum. Methods Phys. Res. Sect. A 764 (2014) 156–166.

[38] I. Bressler, J. Kohlbrecher, A.F. Thunemann, SASfit: a tool for small-angle scattering data analysis using a library of analytical expressions, J. Appl. Crystallogr. 48 (5) (2015) 1587–1598.

[39] G. Kostorz, S.W. Lovesey, Neutron scattering–general introduction, in: G. Kostorz (Ed.). Treatise On Materials Science & Technology, Elsevier, Amsterdam, 1979, pp. 1–67.

[40] C.P. Massey, S.N. Dryepondt, P.D. Edmondson, M.G. Frith, K.C. Littrell, A. Kini, B. Gault, K.A. Terrani, S.J. Zinkle, Multiscale investigations of nanoprecipitate

nucleation, growth, and coarsening in annealed low-Cr oxide dispersion strengthened FeCrAl powder, Acta Mater. 166 (2019) 1–17.

[41] J.D. Casey, A.F. Doyle, R.G. Lee, D.K. Stewart, H. Zimmermann, Gas-assisted etching with focused ion beam technology, Microelectron. Eng. 24 (1) (1994) 43–50.

[42] C. Liu, P.J. Heard, O.D. Payton, L. Picco, P.E.J. Flewitt, A comparison of two high spatial resolution imaging techniques for determining carbide precipitate type and size in ferritic 9Cr-1Mo steel, Ultramicroscopy 205 (2019) 13–19.

[43] L.A. Giannuzzi, J.R. Michael, Comparison of channeling contrast between ion and electron images, Microsc. Microanal. 19 (2) (2013) 344–349.

[44] M. Niederkofler, M. Leisch, 3D-atom probe characterization of nano-precipitates in a PM processed tool steels, Appl. Surf. Sci. 235 (1) (2004) 132–138.

[45] M. Godec, B.Š. Batič, D. Mandrino, A. Nagode, V. Leskovšek, S.D. Škapin, M. Jenko, Characterization of the carbides and the martensite phase in powder-metallurgy high-speed steel, Mater. Charact. 61 (4) (2010) 452–458.

[46] K.C. Hwang, S. Lee, H.C. Lee, Effects of alloying elements on microstructure and fracture properties of cast high speed steel rolls: part I: microstructural analysis, Mater. Sci. Eng. A 254 (1) (1998) 282–295.

[47] Neutron activation and scattering calculator. https://www.ncnr.nist.gov/resource s/activation/, (accessed 2 September 2023.).

[48] E.S. Lee, W.J. Park, J.Y. Jung, S. Ahn, Solidification microstructure and $M_2C$ carbide decomposition in a spray-formed high-speed steel, Metall. Mater. Trans. A 29 (5) (1998) 1395–1404.

[49] V.L. Moruzzi, P.M. Marcus, K. Schwarz, P. Mohn, Ferromagnetic phases of bcc and fcc Fe, Co, and Ni, Phys. Rev. B 34 (3) (1986) 1784–1791.

[50] A. Barron, W. Algozeeb, Physical Methods in Chemistry and Nano Science. Volume 4: Chemical Speciation, MiDAS Green Innovations, Limited, 2020.

[51] C. Körner, Additive manufacturing of metallic components by selective electron beam melting–a review, Int. Mater. Rev. 61 (5) (2016) 361–377.

[52] M. Boccalini, H. Goldenstein, Solidification of high speed steels, Int. Mater. Rev. 46 (2) (2001) 92–115.

[53] M.R. Ghomashchi, Quantitative microstructural analysis of M2 grade high speed steel during high temperature treatment, Acta Mater. 46 (14) (1998) 5207–5220.

[54] S. Zhao, J. Fan, J. Zhang, K. Chou, H. Le, High speed steel produced by spray forming, Adv. Manuf. 4 (2) (2016) 115–122.

[55] N. Saunders, U. Guo, X. Li, A. Miodownik, J.P. Schillé, Using JMatPro to model materials properties and behavior, JOM 55 (12) (2003) 60–65.

[56] G.H. Gulliver, The quantitative effect of rapid cooling upon the constitution of binary alloys, J. Inst. Met. 9 (1913) 263–291.

[57] E. Scheil, Bemerkungen zur Schichtkristallbildung, Int. J. Mater. Res. 34 (3) (1942) 70–72.

[58] P. Kürnsteiner, M.B. Wilms, A. Weisheit, P. Barriobero-Vila, E.A. Jägle, D. Raabe, Massive nanoprecipitation in an Fe-19Ni-xAl maraging steel triggered by the intrinsic heat treatment during laser metal deposition, Acta Mater. 129 (2017) 52–60.

[59] T. Voisin, J.B. Forien, A. Perron, S. Aubry, N. Bertin, A. Samanta, A. Baker, Y. M. Wang, New insights on cellular structures strengthening mechanisms and thermal stability of an austenitic stainless steel fabricated by laser powder-bed-fusion, Acta Mater. 203 (2021) 116476.

[60] R. Wu, W. Li, M. Chen, S. Huang, T. Hu, Improved mechanical properties by nanosize tungsten-molybdenum carbides in tungsten containing hot work die steels, Mater. Sci. Eng. A 812 (2021) 141140.

[61] H. Cui, F. Sun, K. Chen, L. Zhang, R. Wan, A. Shan, J. Wu, Precipitation behavior of Laves phase in 10%Cr steel X12CrMoWVNbN10-1-1 during short-term creep exposure, Mater. Sci. Eng. A 527 (29) (2010) 7505–7509.

[62] M.I. Isik, A. Kostka, V.A. Yardley, K.G. Pradeep, M.J. Duarte, P.P. Choi, D. Raabe, G. Eggeler, The nucleation of Mo-rich Laves phase particles adjacent to $M_{23}C_6$ micrograin boundary carbides in 12% Cr tempered martensite ferritic steels, Acta Mater. 90 (2015) 94–104.

[63] R.W. Cahn, P. Haasen, Physical Metallurgy, 4th ed., Elsevier, Amsterdam, 1996.

[64] X.F. Yu, D.Y. Zheng, X.F. Yang, S.Y. Wang, M. An, G.B. Yan, Y.Z. Xia, F. Xing, Effect of carbide precipitation behavior at high temperatures on microstructure and mechanical properties of M50 steel, J. Mater. Res. Technol. 18 (2022) 1155–1165.

[65] M.E. Thompson, C.S. Su, P.W. Voorhees, The equilibrium shape of a misfitting precipitate, Acta Metall. Mater. 42 (6) (1994) 2107–2122.

[66] M. Nurbanasari, P. Tsakiropoulos, E.J. Palmiere, A study of carbide precipitation in a H21 tool steel, ISIJ Int. 54 (7) (2014) 1667–1676.

[67] J.D. Robson, H.K.D.H. Bhadeshia, Modelling precipitation sequences in power plant steels Part 1–kinetic theory, Mater. Sci. Technol. 13 (8) (1997) 631–639.

[68] A. Inoue, T. Masumoto, Carbide reactions ($M_3C \rightarrow M_7C_3 \rightarrow M_{23}C_6 \rightarrow M_6C$) during tempering of rapidly solidified high carbon Cr-W and Cr-Mo steels, Metall. Trans. A 11 (5) (1980) 739–747.

[69] J. Pilling, N. Ridley, Tempering of 2.25 Pct Cr-1 Pct Mo low carbon steels, Metall. Trans. A 13 (4) (1982) 557–563.

[70] H. Peng, L. Hu, X. Zhang, X. Wei, L. Li, J. Zhou, Microstructural evolution, behavior of precipitates, and mechanical properties of powder metallurgical high-speed steel S390 during tempering, Metall. Mater. Trans. A 50 (2) (2019) 874–883.

[71] E.O. Hall, The deformation and ageing of mild steel: III discussion of results, Proc. Phys. Soc. Sect. B 64 (9) (1951) 747.

[72] N. Petch, The cleavage strength of polycrystals, J. Iron Steel Inst. 174 (1953) 25–28.

[73] R.W. Armstrong, Crystal engineering for mechanical strength at nano-scale dimensions, Crystals 7 (10) (2017) 315.

[74] Z. Li, F. Chai, L. Yang, X. Luo, C. Yang, Mechanical properties and nanoparticles precipitation behavior of multi-component ultra high strength steel, Mater. Des. 191 (2020) 108637.

[75] A. Argon, Strengthening Mechanisms in Crystal Plasticity, Oxford University Press, Oxford, 2007.

[76] A.J. Ardell, Precipitation hardening, Metall. Trans. A 16 (12) (1985) 2131–2165.

[77] R. Lagneborg, Bypassing of dislocations past particles by a climb mechanism, Scr. Metall. 7 (6) (1973) 605–613.

[78] E. Nembach, Precipitation hardening caused by a difference in shear modulus between particle and matrix, Phys. Status Solidi A 78 (2) (1983) 571–581.

[79] Q. Wang, Z. Li, S. Pang, X. Li, C. Dong, P.K. Liaw, Coherent precipitation and strengthening in compositionally complex alloys: a review, Entropy 20 (11) (2018) 878.

[80] L. Sun, T.H. Simm, T.L. Martin, S. McAdam, D.R. Galvin, K.M. Perkins, P.A. J. Bagot, M.P. Moody, S.W. Ooi, P. Hill, M.J. Rawson, H.K.D.H. Bhadeshia, A novel ultra-high strength maraging steel with balanced ductility and creep resistance achieved by nanoscale β-NiAl and Laves phase precipitates, Acta Mater. 149 (2018) 285–301.

[81] W. Xing, F. Meng, R. Yu, A new type of vanadium carbide $V_5C_3$ and its hardening by tuning Fermi energy, Sci. Rep. 6 (1) (2016) 21794.

[82] Y. Liu, Y. Jiang, J. Xing, R. Zhou, J. Feng, Mechanical properties and electronic structures of $M_{23}C_6$ (M=Fe, Cr, Mn)-type multicomponent carbides, J. Alloys Compd. 648 (2015) 874–880.

[83] Y. Luo, H. Guo, J. Guo, W. Yang, Gleeble-Simulated and Semi-Industrial Studies on the Microstructure Evolution of Fe-Co-Cr-Mo-W-V-C Alloy during Hot Deformation, Materials 11 (12) (2018) 2577.

[84] M.M. Serna, J.L. Rossi, MC complex carbide in AISI M2 high-speed steel, Mater. Lett. 63 (8) (2009) 691–693.

[85] C. Kim, V. Biss, W.F. Hosford, A new procedure for determining volume fraction of primary carbides in high-speed and related tool steels, Metall. Trans. A 13 (2) (1982) 185–191.

[86] B. Geng, Y. Li, R. Zhou, Q. Wang, Y. Jiang, Formation mechanism of stacking faults and its effect on hardness in $M_7C_3$ carbides, Mater. Charact. 170 (2020) 110691.

[87] T. Gladman, Precipitation hardening in metals, Mater. Sci. Technol. 15 (1) (1999) 30–36.

[88] M.F. Ashby, Results and consequences of a recalculation of the frank-read and the orowan stress, Acta Metall. 14 (5) (1966) 679–681.